Effect of Ar/N_2 flow ratio on the microstructure and mechanical properties of Ti-Cr-N coatings deposited by DC magnetron sputtering on AISI D2 tool steels

Abdelkrim Kehal [a,b], Nadia Saoula [c,*], Seddik-El-Hak Abaidia [b], Corinne Nouveau [d]

[a] Mechanical Engineering Department, Mouloud Mammeri Tizi-Ouzou University, 15000, Algeria
[b] Physics Department, Research Unity UR-MPE, Boumerdes-University, 35000, Algeria
[c] Center for Development of Advanced Technologies (CDTA), Cité du 20 Août 1956, Baba Hassen, BP n. 17, Algiers, Algeria
[d] Arts et Metiers Institute of Technology, LABOMAP, HESAM Université, F-71250, Cluny, France

Keywords:
Ti-Cr-N
DC magnetron sputtering
Ar/N_2 ratio
Raman
Growing stage

A B S T R A C T

Ti-Cr-N coatings were deposited on Si (100) and AISI D2 tool steel substrates by reactive DC magnetron co-sputtering technique from titanium and chromium target in mixed Ar/N_2 atmosphere. The Ar/N_2 ratio effects on the chemical composition, structure, morphology, intrinsic stress and mechanical properties of the Ti-Cr-N coatings were investigated. The growing process of Ti-Cr-N coatings can be divided into three stages: Stage I, in poisoning mode (low flow ratio $1 < Ar/N_2 \leq 1.4$), Stage II, in transition mode (intermediate flow ratio $1.4 \leq Ar/N_2 \leq 3$) and Stage III in metallic mode ($Ar/N_2 > 3$). For all samples, XRD analysis shown the formation of mixed nitrides phases. In stage I, Ti_2N, $TiN_{0.3}$, and hexagonal-Cr_2N phases were observed. In Stage II, $TiN_{0.3}$, Cr_2N, and cubic-TiN phases were formed, while only TiN and Cr_2N are observed in stage III. The coatings deposited with Ar/N_2 ratio of 3 shows the largest hardness of 24 GPa which is attribute to the dense structure and smoother surface morphology. The properties of the films are discussed in terms of evolution growth stages resulting by the variation of Ar/N_2 flow ratios.

1. Introduction

Binary hard coatings of metal nitrides like TiN and CrN are commonly used as protective coatings in industry because of their high hardness, low friction coefficient and their ability to extend tool life during abrasive and chemical aggressive conditions [1,2]. However, the performance and reliability of these nitrides do not meet the requirements for specific applications such as in high speed machining, dry cutting, drilling and jet engine turbine blades [3]. As a result, ternary nitride coatings such as Ti-Cr-N have attracted great attention due to the combined properties of TiN and CrN. Several research groups [4,5] have shown that the Ti-Cr-N system has good mechanical properties and good chemical stability. Indeed, it has been reported that CrN has a higher corrosion resistance than TiN [6]; Ti-Cr-N is more resistant to corrosion in artificial seawater compared to CrN [7]. Mendoza-Leal et al. [4] found that the coefficient of friction Ti-Cr-N decreases significantly with Cr content. However, with the addition of Cr into TiN to form $Ti_{0.5}Cr_{0.5}N$ coating, the coefficient of friction decreases significantly of 50% than that of TiN [4]. Nainaparampil et al. [8] attributed this low friction coefficient to the plastic deformation of the wear debris when the TiN and CrN were combined into a single film of Ti-Cr-N. Similar results have been reported in the literature where it has been shown that the ternary nitride Ti-Cr-N coating provides the best wear properties [9]. In terms of mechanical properties, it has been observed that the Ti-Cr-N compound coating has higher hardness than that of TiN (21 GPa) and CrN (19 GPa) coatings [5]. The transition from binary CrN to ternary $Ti_{0.2}Cr_{0.4}N_{0.4}$ leads to an increase in hardness from 19 to 24 GPa. With further increase in Ti content, the hardness of ternary $Ti_{0.4}Cr_{0.2}N_{0.4}$ reaches a maximum of 26 GPa [5] In addition to the chemical composition effect, the mechanical properties of ternary nitride-coated steel are influenced by the structure of the coating. For example, it has been shown that the synthesis of ternary coatings generates multiphase structures often resulting in fine-grained and distorted structures [10] and provides ternary nitrides with higher mechanical properties than binary nitrides [11].

According to Musil et al. [12] and Vishnyakov et al. [13], the

* Corresponding author.
E-mail address: nsaoula@cdta.dz (N. Saoula).

microstructure and hardness of the ternary hard coatings are sensitively affected by the energy and density of the ion flux of the plasma. The ion flux consists mainly of Ar^+ and/or N^{2+} ions, whereas, in the case of the DC sputtering, the ionization rate of the sputtered species is typically less than 1% [14]. This indicates that Ar/N_2 flow ratio is expected to be a key factor, which affects not only the film's stoichiometry but also its structure and mechanical properties of the films. Few research groups have reported the effect of the main plasma parameters, such as the effect on the mechanical properties of the Ti-Cr-N films of the variation in discharge power [13,15,16] or the partial pressure of the N_2 flow [11,17,18]. However, to our knowledge, there is no study on the evolution of the properties of Ti-Cr-N thin film related to the Ar/N_2 flow ratio. The effect of this parameter on the properties of the ternary nitride Ti-Cr-N film may be studied. For this purpose, Ti-Cr-N coatings were deposited on Si and AISI D2 substrates using DC magnetron sputtering. During these experiments, we kept all the process parameter constant while varying Ar/N_2 flow ratio. The effect of the Ar/N_2 ratio on the evolution of the deposition rate, structure, chemical composition, and mechanical properties of sputtered Ti-Cr-N coatings were investigated systematically.

2. Experimental

2.1. Samples preparation

In this work, silicon wafers (100) (1×1 cm^2, 450 μm) and AISI D2 steel ($15 \times 15 \times 5$ mm^3) were used as substrates. The chemical composition of AISI D2 steel is 1.6C, 0.35 Mn, 12 Cr, 0.25 Si, 0.5 Ni, 0.9 Mo, 0.5 V and Fe balance, in weight percent (wt%). The steel samples were subjected to heat treatment in order to increase their hardness. A Rockwell C hardness of 55 HRC was obtained after the heat treatment, and the working faces of the substrates were polished with silicon carbide papers ranging from (180 to 800 grit). The average surface roughness of the polished substrates was Ra = 90 nm. Before the deposition process, the substrates were cleaned and rinsing in an ultrasonic bath of acetone and then dried. Then, the substrates were loaded into the rotating substrate holder inside the deposition chamber.

2.2. Deposition of coatings

The Ti-Cr-N coatings were deposited by DC reactive magnetron sputtering (KENOSISTEC - model KS40V - 113K12). Ti-Cr-N films were obtained by co-sputtering of titanium and chromium targets (with a purity of 99.9% and a size of $408 \times 127.5 \times 7.5$ mm^3). High purity Ar (99.999%) and N_2 (99.999%) gas were introduced during the deposition process. The distance between the targets and the vertical rotating substrate-holder is 105 mm. The substrate-holder rotates in an oscillatory motion between the target of Ti and Cr at a speed of 3 rpm. The number of oscillations for each deposition was fixed to 151 cycles, resulting in uniform coating thickness. The chamber was evacuated to a base pressure of $\sim 1.5 \times 10^{-6}$ mbar. In order to remove the surface oxide or any contamination, the targets and the substrates were cleaned by ion etching in Ar plasma discharge.

The sputtering conditions were set at two different applied powers: 1500 W and 3000 W for the chromium and titanium targets, respectively. The deposition time was 22 min. The temperature of the substrate during the deposition was about 100–140 °C. Different Ar/N_2 gas mixtures were used and the total working pressure was fixed to 3×10^{-3} mbar.

2.3. Coatings characterization

The coatings were analysed to investigate their structural, morphological and mechanical properties. X-ray diffraction (XRD) and Raman spectroscopy were used to identify the structure of the coatings. The X-ray diffraction was carried out using a Philips System X'Pert diffractometer with CuKα radiation (λ = 1.541 Å) in Bragg-Brentano configuration (θ-2θ). The diffractometer acquiring range is between 15° and 90°, using a scanning speed of 3.55°/min and a precision of 0.03°. The Raman spectra of the coatings were recorded on a Horiba LabRAM HR spectrometer using the 633 nm line of Ar^+ Laser as an excitation source. The spectra were recorded over the range of 50 to 1300 cm^{-1}.

The surface morphology of the coatings was observed with a JEOL field emission scanning electron microscope FE-SEM (JEOL JSM 7610F). The composition of the coatings was determined by dispersive energy X-ray spectroscopy (EDS operated at 5 kV). The coating's thicknesses were measured from cross sectional scanning electron microscopy (SEM) micrographs. The surface roughness of the films was determined by the MFP-3D from Asylum Research atomic force microscopy (AFM).

To determine the residual stress, thin rectangular sheets of silicon Si (100) ($25 \times 10 \times 0.38$ mm^3) were used as substrates. The curvature radius was measured by the optical profilometer (VEECO, Wyko NT-1100) before and after the Ti-Cr-N deposition. The values and the directions of the curvature radii were obtained by Gwydion software, which determines the curvature of a surface with two orthogonal directions. The residual stress was then calculated using the modified Stoney formula [19].

The hardness of the nitride coatings was measured by a nano-indentation tester CSM module with Berkovich diamond indenter tip under a fixed load of 2 mN. In the nano-indentation test, the maximum penetration depth of the indentation should not exceed 10% of the thickness of the film to avoid the influence of the substrate. Multiple indentations were made at different locations on the film's surface. The hardness and Young's modulus were then determined by the Oliver and Pharr method [20].

3. Results and discussion

3.1. Chemical composition and deposition rate

The chemical compositions of the Ti-Cr-N coatings determined by EDS analysis are listed in Table 1. The results confirm the presence of nitrogen, chromium and titanium in the coatings. It should be also noted that in all the coatings, the presence of oxygen (up to 11.5 at.%), which is possibly due to the adsorbed residual oxygen during deposition [21]. Also, the results indicates that increase in Ar/N_2 ratio results in decrease of the content of N atoms in the coatings from about 36 to 13.5 at.%. The Cr/Ti atomic ratio in the coatings stays nearly constant in the range of 0.87–1.16.

Fig. 1 shows that the nitrogen ratio to metallic species (N/Ti + Cr), decreases with the increase of the Ar/N_2 ratio. Fig. 2 shows the correlation between the deposition rate and the concentration of nitrogen and oxygen as a function of the Ar/N_2 ratio. The amount of oxygen observed in all samples of the coatings is relatively constant, except for the coatings deposited in the atmosphere of $Ar/N_2 = 2$ where the samples contain a higher amount of oxygen. The cross-section analysis (Table 1) clearly show that the thickness increased with the Ar/N_2 ratio, from 750 nm to 1310 nm. This ratio has a significant effect on the deposition rate. This effect is a well-known for the reactive sputtering process. Indeed, at the lower Ar/N_2, the process deposition is in poisoning mode. With the increase of Ar/N_2 flow ratio, the overall sputtering yield of the target increases. Under these conditions, the process is in metallic mode [22] and the deposition rate of metallic-mode is nearly 1.76 times that of poisoned-mode. There is also an intermediate Ar/N_2 regime (from 1.4 to 3) that indicates a simple transition between the metallic and poisoned modes. From these observations, the composition of the film is the result of the competition between two processes: (i) the quantity of metallic species (Ti + Cr) arriving from the target related to its sputtering yield, and (ii) the flow rates of reactive gases Ar/N_2. To illustrate this dependence, the growing process of Ti-Cr-N coatings can be divided into three stages (Fig. 2). Stage I corresponds to a high nitrogen concentration with

Table 1
Film thickness, composition, metal concentration ratio, atomic ratio, and film stoichiometry as a function of Ar/N_2 ratio.

Ar/N_2 ratio		Thickness (nm)	Elemental composition (at.%)					Atomic ratio			Film stoichiometry $(Ti_xCr_{1-x})\ N_y$
			Cr	Ti	O	N	Cr + Ti	Cr/Ti	X = Ti/(Ti + Cr)	Y=N/(Ti + Cr)	
40/40	1.0	750	28.6	28.8	6.6	36.0	57.4	0.99	0.50	0.62	$(Ti_{0.50}\ Cr_{0.50})\ N_{0.62}$
47/33	1.4	1088	28.0	32.0	5.0	35.0	60.0	0.87	0.53	0.58	$(Ti_{0.53}\ Cr_{0.47})\ N_{0.58}$
54/26	2.0	1070	34.0	32.0	11.5	22.5	66.0	1.06	0.48	0.34	$(Ti_{0.48}\ Cr_{0.52})\ N_{0.34}$
60/20	3.0	1200	35.4	39.0	6.8	18.8	74.4	0.90	0.52	0.25	$(Ti_{0.52}\ Cr_{0.48})\ N_{0.25}$
64/16	4.0	1310	43.0	37.0	6.5	13.5	80.0	1.16	0.46	0.17	$(Ti_{0.46}\ Cr_{0.54})\ N_{0.17}$

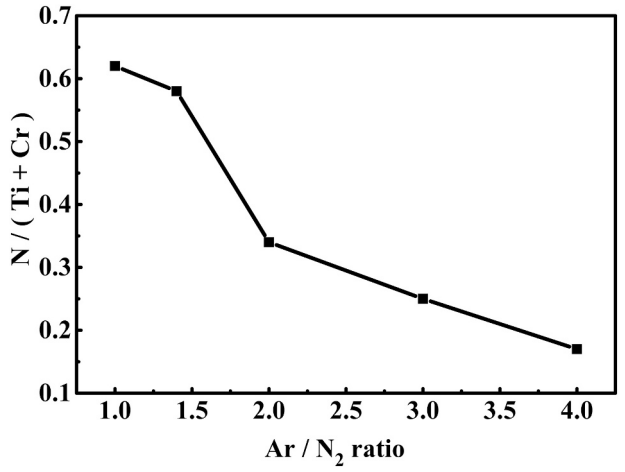

Fig. 1. The N/(Ti + Cr) ratio of the Ti-Cr-N films deposited with different Ar/N_2 flow ratios.

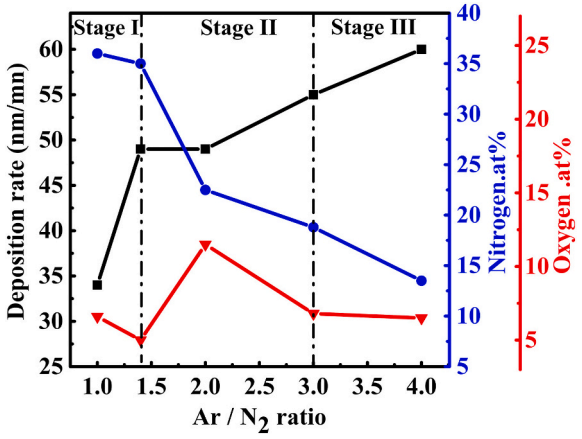

Fig. 2. Deposition rate, nitrogen and oxygen content deposited with different Ar/N_2 flow ratios.

a low deposition rate and a low oxygen concentration. Stage II corresponds to an intermediate nitrogen concentration and deposition rate with a high oxygen concentration; and Stage III corresponds to a low nitrogen concentration, a high deposition rate, and a low oxygen concentration. This behaviour can be defined in more details as follows:

Stage I corresponds to the lower gas ratio (from $Ar/N_2 = 1$ to 1.4). Two phenomena predominate. Firstly, the high collision frequency of particles species in the plasma caused by the high molecular diameter of N_2 ($\Phi = 3.14$ Å) or N^{2+} ions in gaseous phase compared to the Ar atoms ($\Phi = 1.76$ Å) or Ar^+ ions ($\Phi = 1.54$ Å) [23]. Secondly, the formation of a ceramic compound on the target surface (poisoning mode deposition) [24]. Under these conditions, the high amount of N_2 molecules induces more collisions, which leads to increase the molecules dissociation and the formation of N^+ ions. These finally will be implanted into the film [25]. Consequently, the deposition rate is lower in this first stage, because of the poisoning of the target. For the presence of oxygen, this element is at its lower level. Thus, the efficiency of removal of the surface oxygen by the nitrogen ions in this regime is almost identical to the ions flux dominated by the argon ions gas as mentioned by Vishnyakov et al. [13].

Stage II (from $Ar/N_2 = 1.4$ to 3) corresponds to the transition mode (intermediate in the values of the deposition rate and nitrogen concentration). The mean free path of the sputtering argon gas increases as the nitrogen flow rate decreases [25]. Under these conditions, the collision frequency between sputtered particles and sputtering gas molecules is lower. The deposition rate was found almost constant. According to Patsalas et al. [26] increasing ion flux (below the subplantation threshold) can in certain conditions decrease the deposition rate and provide enough time for the migration of adatoms and so increases their surface diffusion length without increasing the thickness. The content in nitrogen decreases from 35 to 22.5% while the oxygen content increases from 5 to 11.5%. These results are consistent with the fact that in the pressure range studied in this stage, the sputtering yield increases with the pressure, but the pressure is not high enough to promote a denser film with vertical growing and less oxygen contamination. However, the sputtering pressure is well known to be efficient in inhibiting the adsorption of oxygen if it is used at an appropriate level of flow rate.

In the stage III, the flow and energy of ions flux of sputter-ejected species increase further as the Ar/N2 ratio (>3) increases. As a result of the substantial increase in deposition rate, the adsorbed oxygen impurities can be easily re-sputtered by the incident ions particles, especially Ar^+ [21] however, the concentration of oxygen decreased to 6.2 at.% for $Ar/N_2 = 4$. Finally, since the chemical composition and velocity of the deposited species play a significant role in the film properties, these stages are important for the following discussion.

3.2. *Structure analyses*

The X-ray diffraction patterns of Ti-Cr-N films deposited using

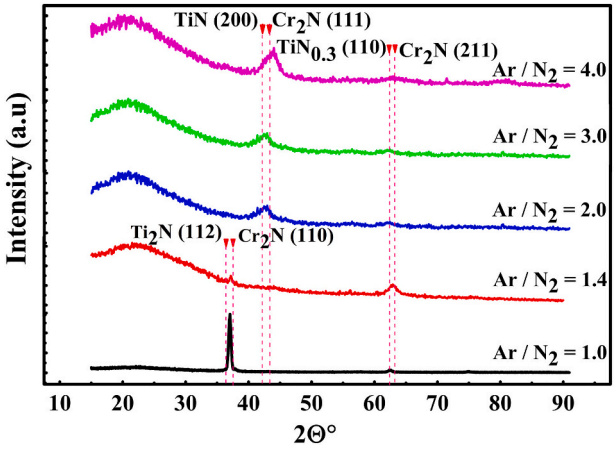

Fig. 3. XRD patterns of Ti-Cr-N films deposited with different Ar/N_2 flow ratios.

various Ar/N_2 ratios are shown in Fig. 3. All patterns display a broad peak at a diffraction angle of about 22°, suggesting an amorphous-like phase. The XRD reflections indicate a presence of binaries nitrides of (Ti_2N, $TiN_{0.3}$ and Cr_2N) and their reflections are overlapped to a single large peak. This suggests a good solubility of these binaries nitrides as the Ar/N_2 ratio was increased [27]. Furthermore, no peaks referring to the oxide phase were observed by XRD, implying that oxygen could be present in the grain boundaries and/or forming an amorphous oxide phase [28].

In stage I (from $Ar/N_2 = 1$ to 1.4), the Ti-Cr-N films contain predominantly a mixture of two rich metallic nitrides Ti_2N (112) and Cr_2N (110) orientations, with a small volume fraction of another mixture of $TiN_{0.3}$ (110) and Cr_2N (211) crystalline orientations. When the Ar/N_2 ratio increases to 1.4, the [$TiN_{0.3} + Cr_2N$] diffraction peak increase and the peak of [$Ti_2N + Cr_2N$] tends to disappear. Moreover, the width of the diffraction peak increases and its intensity decreases suggesting increased stresses in the coating and a decrease in the grains size [29].

For the film deposited at the transition stage ($Ar/N_2 = 2$), the dominant texture is composed of cubic TiN (200) and hexagonal Cr_2N (111) phases. The distortion mechanism, caused by the transition phase of the Ti-N in a mixture with Cr_2N, led to the interstitial insertion of the nitrogen atoms into the hexagonal structure of $TiN_{0.3}$ (a = 2.9737, b = 2.9737, c = 4.7917 Å) resulting in a distorted fcc-TiN, i.e. with a large lattice parameter (a = b = c = 4.2417 Å) [30]. However, with dense grain boundaries this can indicate that compressive stress occurred within the coating at $Ar/N_2 = 2$.

At higher energies of incident ions of the third stage, (from $Ar/N_2 = 3$ to 4), the grains grow with the [$TiN + Cr_2N$] predominated orientation. A clear increase in the width of the peak can be observed (Fig. 3), indicating a decrease in the grain size and an increase in defect density due to enhanced collisions of incident particles with the coating surface, which is likely to lead to the generation of high intrinsic stresses during the growing film [31].

In all the films, it could be observed the chromium nitride Cr_2N in the solid solution (Ti,Cr)N, whereas, the titanium nitride which coexists with Cr_2N phase, evolves toward three phases: Ti_2N, $TiN_{0.3}$ and TiN. This could be explained by the enthalpy formation of the nitride of Cr and Ti ($\Delta H_{TiN} = -337.65$ kJ/mol and $\Delta H_{CrN} = -117.15$ kJ/mol), which shows that the Ti-N is easier to be formed than Cr-N [32].

3.3. Raman spectroscopy

In order to confirm and obtain additional information about the different observed phases in XRD patterns, the structure of Ti-Cr-N coatings was analysed by Raman spectroscopy in the range between 50 and 1200 cm^{-1}. The Raman spectra of the obtained coatings are presented in Fig. 4.

The Ti-Cr-N Raman spectrum is similar to those collected for Ti-N [33] and Cr-N [34] from 50 to 720 cm^{-1}. This indicates that the substitutional solid solution of Cr in TiN does not affect the Raman spectra significantly. A similar observation was reported for the Raman spectra of Ti-Cr-B-N [35] and Al-doped TiN films [36]. In addition, this confirms the results of the XRD patterns where the (Ti-N) system seems to be more sensitive to the variation of the Ar/N_2 ratio than the stable (Cr_2N) phase.

However, the Raman spectrum of Ti-Cr-N film can be deconvoluted into six Gaussian peaks. Table 2 gives the derived wavenumbers for the TA, LA, TO or LO modes of Ti-Cr-N coatings.

The low-frequency scattering caused by acoustical phonons (TA and LA modes) is related to vibrations of the heavier metal atoms, while optical range scattering (TO and LO) refers to vibrations of the lighter non-metal ions [37]. Furthermore, an increase in the intensity of the optical phonon band suggests the formation of metallic vacancies, while an increase in the intensity of the acoustical band indicates a nitrogen vacancy [38]. In comparison to the binary TiN and CrN, the Raman spectra of the Ti-Cr-N coating show the existence of a broad peak with low intensity corresponding to the second-order transitions (A + O) at the range of 740 to 795 cm^{-1}, which is in good agreement with those reported by Mehr et al. [18]. At 52 cm^{-1}, all spectra present a very weak line that corresponds to the laser plasma line. This line is used to calibrate the frequency of the Raman shift [39].

The study of the intensity ratio of the nitrogen peak to metallic peak I = (TO + LO) / (TA + LA) is a semi-quantitative method to analyse the variations in vacancy concentrations [38]. It is obvious from Fig. 5 that the Raman spectra of the different films are affected by the flux of ions and the ion energy caused by the variation of the Ar/N_2 ratio. In addition, Fig. 5 show that the global tendency of the scattering intensity decreases as a function of the increase of the Ar/N_2 ratio. This indicates that the crystalline phase is decreasing [35,40], while the metallic phase is increasing continuously with the Ar/N_2 ratio. This is in perfect consistency with chemical results (Table 1). Due to the high reflectivity of the metallic surfaces, the incident light penetration depth limits the

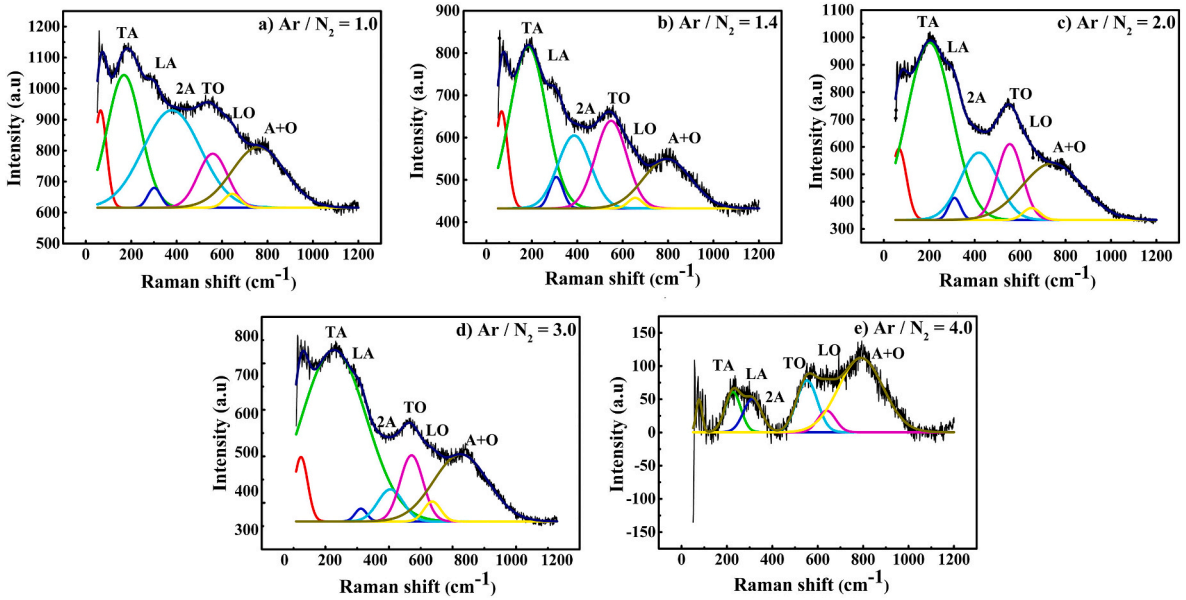

Fig. 4. Raman spectra of Ti-Cr-N films deposited at the Ar/N_2 flow ratio a) 1, b) 1.4, c) 2, d) 3 and e) 4.

Table 2
Summary of assignments for the acoustic and optic phonon modes (cm^{-1}) and relative intensity ratio of $I_{(TO+LO)}$ / $I_{(TA+LA)}$ for the Ti-Cr-N films.

Ar/N_2 ratio	Intensity (a.u.)								$I_{(TO+LO)}$ / $I_{(TA+LA)}$ ratio
	TA	LA	2A	TO	LO	A + O	$I_{(TO+LO)}$	$I_{(TA+LA)}$	
1.0	1043.6	679.8	930.0	789.9	660.6	811.8	1450.5	1723.4	0.8415
1.4	816.0	506.7	604.8	639.6	457.3	549.2	1096.9	1322.7	0.8293
2.0	981.6	413.5	579.0	610.2	376.8	539.8	987.0	1395.1	0.7074
3.0	764.6	354.9	404.8	492.6	373.3	495.1	865.9	1119.5	0.7734
4.0	60.9	50.6	Not observed	78.2	32.8	112.1	111.0	111.5	0.9958

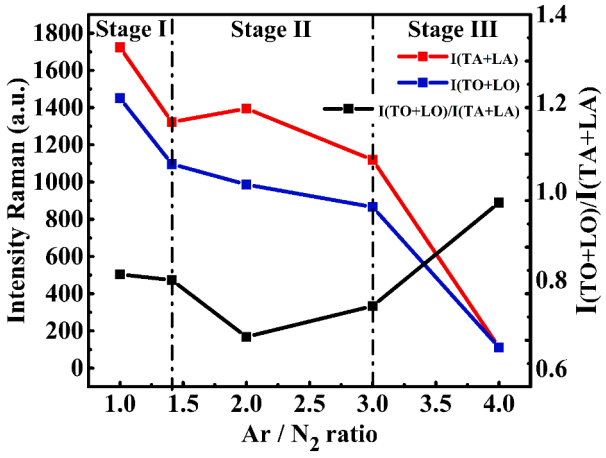

Fig. 5. Dependence of the intensities $I_{(TA+LA)}$, $I_{(TO+LO)}$ and relative intensities $I_{(TO+LO)}$ / $I_{(TA+LA)}$ of Ti-Cr-N films on Ar/N_2 flow ratios.

Raman scattering in the case of the metallic materials; which consequently reduces the intensity in the Raman spectra as the Ar/N_2 flux increases [41]. The variation of the intensity ratio I = (TO + LO) / (TA + LA) can be explained as follows: in stage I, the intensity ratio I = (TO + LO) / (TA + LA) changes slightly from 0.8415 (at $Ar/N_2 = 1$) to 0.8293 (at $Ar/N_2 = 2$) which corresponds to a slight decrease in nitrogen content from 36 to 35 at.% (Table 1). In the second stage (Fig. 5), the intensity ratio I = (TO + LO) / (TA + LA) reached the minimum value of 0.7074 at $Ar/N_2 = 2$, which corresponds to a higher reduction in nitrogen content (from 35 to 22 at.%) and the (Ti + Cr) increased continuously with the Ar/N_2 ratio (Table 1). However, it should be noted that the intensity ratio of I = (TO + LO) / (TA+LA) = 0.7074 at the $Ar/N_2 = 2$, should normally be at intermediate values between 0.8293 and 0.7734 in order to express the continuous decrease of the nitrogen content analysed by EDS (Table 1). The intensity ratio I = (TO + LO) / (TA + LA) of 0.7074 represents the transition zone between the poisoning mode and the metallic mode as a function of the Ar/N_2 ratio. For the third stage (Fig. 5), the intensity ratio I = (TO + LO) / (TA + LA) increases further more at $Ar/N_2 = 4$ while we observe an opposite tendency with the nitrogen content. An increase in the nitrogen peak Raman intensity will imply the formation of metallic vacancies, as described above. This can be explained by the increase of the concentration of titanium vacancy in the films because of the preferential re-sputtering phenomenon of Ti observed at the higher ions flux (gas ratio = 4) (Table 1). Under these conditions, the Ti vacancies with N atoms as their first nearest neighbours, contribute to the rise in the optical scattering [40], which is observed in Fig. 4e.

3.4. *Microstructure and morphology*

The microstructure and surface morphology of the Ti-Cr-N coatings on (Si) substrates are shown in Fig. 6. The SEM micrographs show that the coatings have the typical columnar structure that is expected for PVD coatings. The cross-section SEM images of the Ti-Cr-N coating show a clear evolution of the thickness with the Ar/N_2 ratio. The surface morphology evolves into two main forms: from 1 to 1.4 of Ar/N_2, the surface morphology is pyramidal (Fig. 6f and g) and presents the greatest surface roughness RMS = 4.4 nm at $Ar/N_2 = 1.4$. When the gas flow ratio increases from 2 to 4, the coatings exhibit a cauliflower-like structure (Fig. 6h, i and j) and smoother surface with a low surface roughness of RMS = 1.9 nm obtained at $Ar/N_2 = 3$.

Based on the three stages of transition mentioned above, the evolution of the morphology and microstructure of the Ti-Cr-N coatings can be interpreted as follows:

Stage I ($Ar/N_2 = 1$ to 1.4): the evolution of the growing structure is governed by the coarsening of the columns structure, resulting in deep cups between columns and open column boundaries in combination with the atomic shadowing effect [42]. For this stage, a slight increase in roughness from 3.8 nm to 4.4 nm was noticed (Fig. 7). The width of the columnar grains increases with a faceted surface. At this early stage, we can see that the thickness increases by more than 30% from 750 to 1088 nm (Fig. 6a and b). However, this behaviour can be related to the limited penetration of particles at the top of the layer [26], which could be due to the insufficient ion energy to densify the surface growing film.

At the second stage, from $Ar/N_2 = 1.4$ to 3; the roughness decreases when the flow ratio increases. This indicates the beginning of the densification and smoothening of the films. The transition from roughening mechanism, due to the limited mobility of surface defects (Stage I) [37] to the smoothing mechanism controlled by the surface diffusion effect (Stage II) [43] is clearly demonstrated by the disappearance of the faceted surface (Fig. 6h). Both of these opposite effects of roughening-smoothing are associated with surface energy, as the thin film growth the system tends to form the most energetically favourable configuration [44]. However, the increase in the Ar/N_2 ratio induces a higher surface diffusion that allows the adatoms to avoid the direct sticking on the top of the columns and diffuse superficially and efficiently, filling in more the voids between them, resulting in the disappearance of the faceted surface [28]. Compared to the first stage, where the deposition rate lags the process of the surface diffusion [45], the slight decrease in thickness (deposition rate) at the second stage ($Ar/N_2 = 2$) (Fig. 6h) indicates the beginning of the densification of the film under the increase in ion bombardment [46]. The smoother surface obtained at $Ar/N_2 = 3$, indicates that the optimum or/and the critical energy delivered to the growing film per deposited particle was reached [47]. According to Dubey et al. [48] the bombardment of the growing film surface with a certain critical threshold of kinetic energy during the deposition process of a sputter atom results in the non-penetration of ions beyond the first atomic layer. Then their energy is essentially transferred to the adatoms, thereby increasing the surface mobility, the surface diffusion reaching its maximum and decreasing the surface roughness to its lower RMS = 1.9 nm.

At the third stage, $Ar/N_2 > 3$, the sputtered atoms induced by the increase of the gas ratio to 4 arrive at the surface of the growing film with enhanced energy, corresponding to a change from smoothing to a roughening mechanism. The surface roughness RMS increases from 1.9 to 2.7 nm, which could be attributed to the bulk displacements of adatoms and the re-sputtering of the near-surface atoms [48]. The result of chemical analysis (Table 1) confirms that the process of growing film under this stage was enlarged by preferential re-sputtering of the lighter

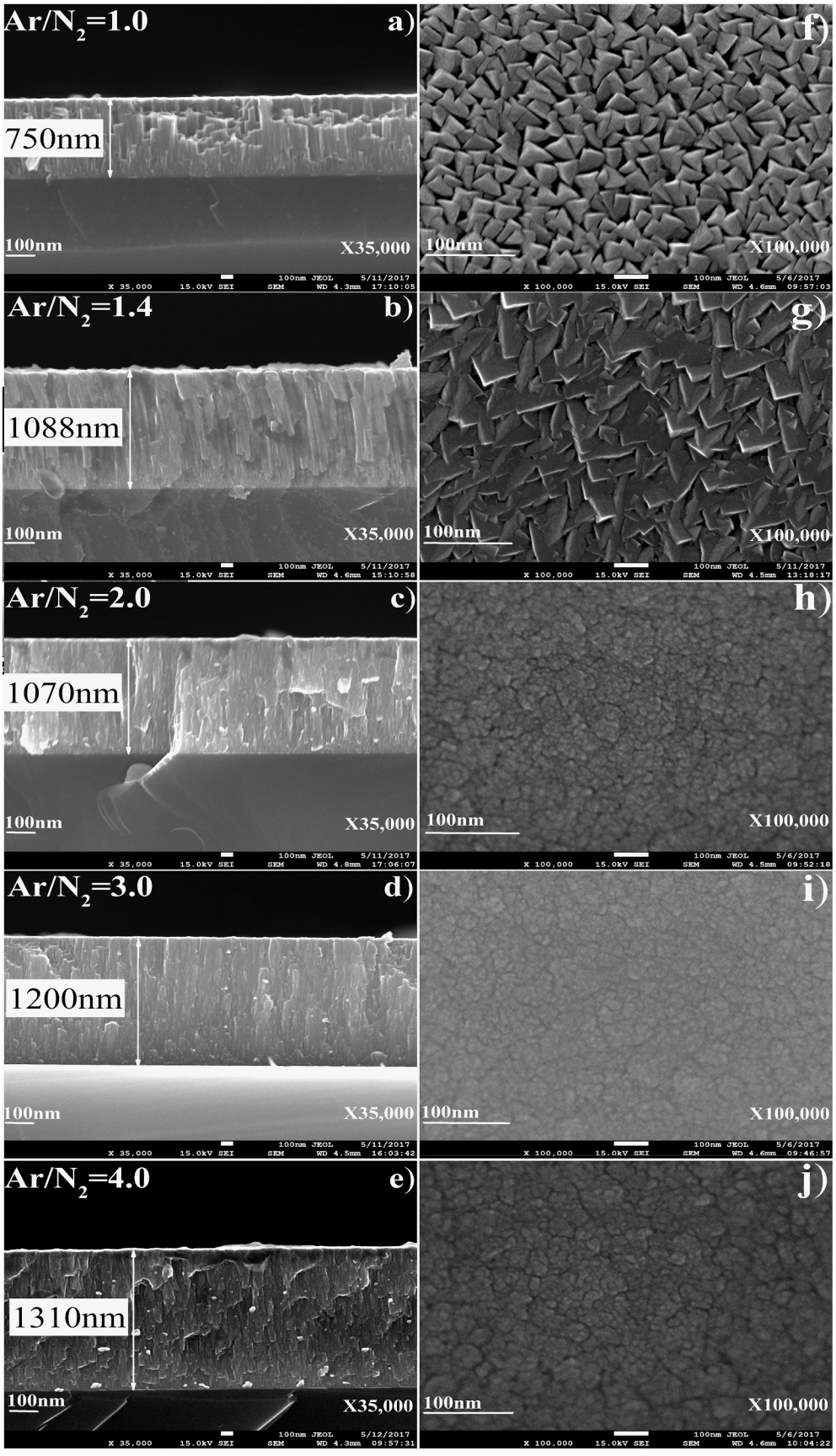

Fig. 6. FE-SEM cross-section and surface morphology of the Ti-Cr-N coatings deposited with different Ar/N_2 flow ratios.

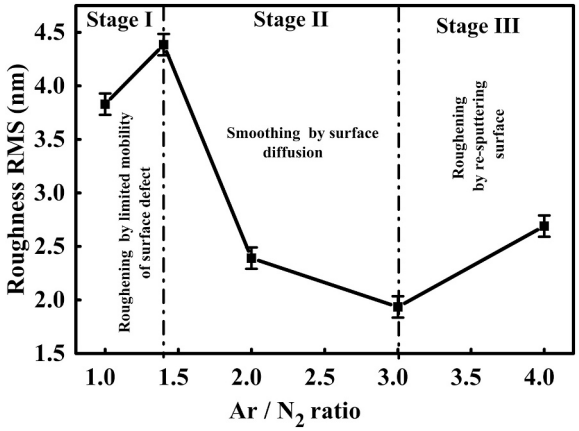

Fig. 7. Surface roughness RMS of the Ti-Cr-N films deposited with different Ar/N_2 flow ratios.

titanium atom [49], which decreases the content of titanium from 39 to 37 at.% at $Ar/N_2 = 4$, resulting in surface defects and roughening of the film surface.

3.5. Residual stress

The Stoney formula was used to calculate the residual stress σ in the coatings:

$$\sigma = \frac{1}{6}\left(\frac{1}{Ra} - \frac{1}{Rb}\right)\frac{Et_s^2}{(1-\nu)t_f} \quad (1)$$

where E, is the Young's modulus (181 GPa) of the substrate, ν the Poisson's ratio (0.28) of the substrate, t_s the thickness of the substrate, t_f the thickness of the film, R_b and R_a the curvature radii of the substrate before and after deposition, respectively [19].

As shown in Fig. 8, the stress in all films is compressive, and tends to be proportional to the deposition rate, except at $Ar/N_2 = 3$, then it increases for a flow ratio = 4.

According to the results obtained by Stoney formula, the increase in the residual compressive stress is more affected by the deformed shape related to the curvature than the conthing's thickness. These two dimensional factors (thickness and the radius of curvature) are inversely proportional in our study, i.e. that the induced compressive surface stress pulls the surface outwards, making the curvature of film/substrate system more convex; the radii of the convex shape of substrate tends to

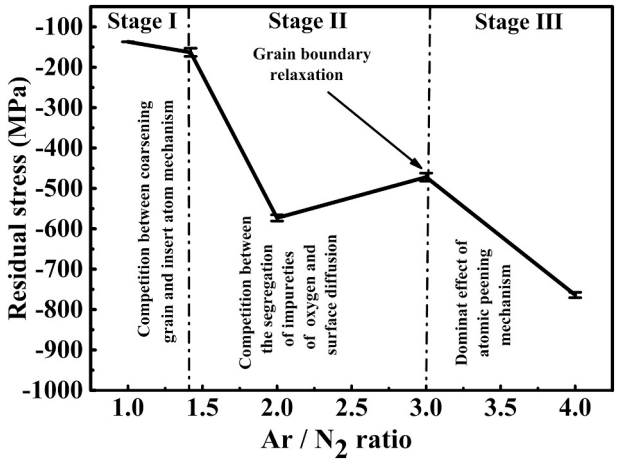

Fig. 8. Residual stress of Ti-Cr-N films deposited with different Ar/N_2 flow ratios.

decrease, which leads to increase further more the residual compressive stress with the higher atomic mobility induced by the increase in Ar/N_2 ratio.

However, the total residual stress can be considered as a result of dynamic competition between the tensile and compressive stress developed during growth of the film [50]. To understand the stress data, the morphology structure-stress relationship is studied fellow as function of the stage mentioned above:

Stage I (from $Ar/N_2 = 1$ to 1.4); the grain size and thickness of the films increase and the stresses are compressive. The increase of the column size caused by the coarsening grains boundary mechanism (Fig. 6a and b), usually induces tensile stress [51], while the total intrinsic stress calculated by the Stoney formula is compressive (increases from -136 ± 0.1 to -162 ± 10 MPa at $Ar/N_2 = 1.4$). This proves that the tensile stress induced by the reduction of the grain boundaries was competed by another mechanism that generates a significant compressive stress state. According to the models proposed by Sheldon et al. [52], the tensile and compressive mechanisms can be both operating during the film growth. Indeed, the tensile stress occurring at the early stage of the film coalescence and post-coalescence, can be compensated by the compressive stress induced by the insertion of extra atoms to the grain boundary leading to a compressive stress state. This can explain, that the final residual stress state of the 1088 nm thick film, is the result of the dominant contribution of the inserted extra atoms against the coarsening grain boundary mechanism during the film growth.

Stage II (from Ar/N_2 = 1.4 to 3); we observe an increase in compressive stress, from -162 ± 10 to -615 ± 8 MPa at $Ar/N_2 = 2$. This could be explained by the competition between the tensile stress induced by the increase in surface mobility of the adatoms [53] and the stress induced by the insertion of oxygen atoms into the grains boundary [54]. However, the effect of the segregation mechanism of oxygen atoms on the grain boundary is dominant and tends to be contrasted with the tensile stress state by restricting the length of the surface diffusion at the very early stage of the film growth. The result is a compressive macro-stress state in the film at Ar/N_2 = 2. Then, the increase in the ions flux of the sputtered atoms/ions at Ar/N_2 = 3 leads to reach the threshold energy of deposition. The surface diffusion becomes dominant which allows the films layers to grow in quasi-two-dimensional growth mode. Consequently, the adsorption of oxygen and the point defects were reduced. Indeed the annihilation of Frankel pairs or the annihilation of interstitials were found to be relaxed on the surface growing film [55]. During this process, the distance between the columns leads to the development of attractive interatomic forces through the interstices, i.e. tensile stress in the film. Below the critical inter-column distance, the repulsive forces generated between the cylindrical structures will play a predominant role and the resulting residual stresses will remain in the compressive state [56]. In other studies, this phenomenon of evolution in stress is called “grain boundary relaxation” or “grain boundary shrinkage” [56].

Finally at the third stage ($Ar/N_2 > 3$), the oxygen impurities were reduced at a relatively constant level. The compressive stress at $Ar/N_2 = 4$ increase from -499 ± 10.6 to -798 ± 7 MPa, this can be related to knock-on (or atomic peening) processes [57]. According to the model of Davis et al. [57] and Windischmann et al. [58], if the energy of the deposited particles species exceeds the threshold of the critical energy, the ions or atoms deposited at the surface will penetrate into the structure and result in the increased defects. In this case, the compressive stresses can be caused by the direct effect of the subplantation ion of bombarding species in the films and the displacement of atoms from a lattice of the film to interstitial positions [59].

3.6. Mechanical properties

Hardness is defined as the resistance of the material to plastic deformation and is mainly sensitive to compressive stress, grain size,

preferred orientation and defect density [60]. The Young's modulus is considered as a measurement of the stiffness of the material and it's variation is consistent with the hardness of the coating [61]. The hardness (H), Young's modulus (E) and H^3/E^2 ratio of the Ti-Cr-N coatings are shown in Fig. 9. All of the coatings are much harder than the uncoated AISI D2 substrate (6.4 GPa). The hardness of the coatings ranges from 10 to 24 GPa. The maximum hardness was achieved for the coating deposited at $Ar/N_2 = 3$. The same trend was observed for Young's modulus ranging from 190 to 255 GPa with a maximum observed for Ar/N2 = 3. Further increase in ions flux to Ar/N2 = 4, results in a decrease in hardness and Young's modulus to 15 GPa and 245 GPa, respectively. These values of hardness and Young's modulus are in agreement with the results obtained by other studies (Table 4) [16,62–65].

The evolution in hardness and Young's modulus of Ti-Cr-N films can be related to solid solution hardening, lattice distortion, densification/strengthening mechanism of the grain boundaries and the nature of chemical bonding strengthening. The effect of these factors on the mechanical properties can be explained as follows:

At the first stage, from $Ar/N_2 = 1$ to 1.4, the minimum hardness was observed for the films with a similar amount of chromium and titanium (Table 1) obtained at $Ar/N_2 = 1$. Similar results were reported by Hones et al. [66]. In terms of structure, this corresponds to the preferred orientation related to the coexistence of two metallic rich nitrides (Ti_2N + Cr_2N) phases. This ($Ti_2N + Cr_2N$) peak tends to disappear at a gas ratio of 1.4 when the peak intensity of the solid solution ($TiN_{0.3}$ + Cr_2N) further increases. As a consequence, the hardness increases from 10 to 13 GPa at $Ar/N_2 = 1.4$ indicating the beginning of the hardening by the mixed multi-phase structure [63]. However, the ceramics in mixed phases are well known to have a higher hardness than each phase on its own [67].

In the second stage, when the Ar/N_2 ratio is increased from 1.4 to 2 a higher strength of the material was observed. This may be due to the combined effect of two parameters. The first is a greater increase in compressive stress induced by impurity segregation of oxygen into the grain boundary, and the second is a distortion mechanism caused by the transition phase of the (Ti-N) in a mixture of Cr_2N. However, the interstitial insertion of the nitrogen atoms into the hexagonal structure of $TiN_{0.3}$ results in a distorted fcc-TiN [30]. This mechanism accompanied by the expansion in lattice parameter contributes to the enhancement of hardness by a dislocation blocking effect [68]. As mentioned above, for the Ar/N_2 ratio of 3, the surface diffusion is at its maximum level. In this state, two processes can be produced and contribute to reach the maximum in mechanical properties of the film: (i) according to Carter et al. [69] the surface diffusional relaxation process leads to maximise neighbour bonding between atoms, whereas the decrease in the interatomic distance was related to the covalent band gap in an inversely proportional way. The higher energy of the covalent bonding led to stronger interatomic forces and contributes to the improvement in film hardness [70]; (ii) the second process is the reduction of the fraction of grain boundary voids, thereby strengthening the grain boundaries mechanism [46]. Finally, the result is the improvement of the hardness of (TiN + Cr_2N) structure by the densification of the film and strengthening mechanism of the grain boundaries.

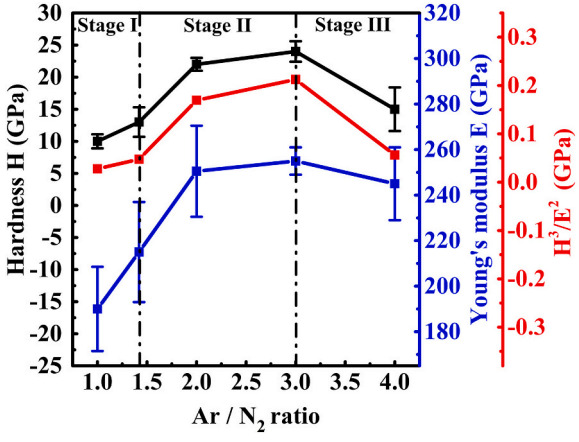

Fig. 9. Hardness, Young's modulus and plastic deformation resistance (H^3/E^2) ratio of the Ti-Cr-N films deposited with different Ar/N_2 flow ratios.

In the third stage ($Ar/N_2 > 3$), the hardness dropped to 15 GPa. This can be explained by two factors: first, an increase in the metallic character of the bonding due to a decrease in nitrogen content and thus a decrease in its covalency [71], and second, excessive densification caused by higher ion bombardment. According to Su et al. [72], the increase of the hardness in thin films is affected by high compressive stress. Therefore, proper stress may be required to obtain a higher hardness. Otherwise, the material may undergo a plastic flow, and a reduction in hardness will occur if the energy of incident ions exceeds the critical level of energy. Besides hardness and elastic modulus, the ratio H^3/E^2 is also important to evaluate the resistance of the coating to plastic deformation in loaded contact [73]. From the nanoindentation data, the plastic deformation resistance (H^3/E^2) of Ti-Cr-N films was calculated and the values are presented in Table 3. The (H^3/E^2) is related to the surface plastic deformation response to sliding contact load, which was associated with the hardness [74]. According to the nanoindentation data (Table 3), a higher hardness corresponds to a higher H^3/E^2 ratio, which is an indication of higher plastic deformation resistance for the film obtained at $Ar/N_2 = 3$. As a result, high hardness and low elastic modulus are desirable, as it allows the load to be distributed over a wider area and therefore a good improvement wear resistance [75].

4. Conclusion

Titanium chromium nitride films were deposited on Si (100) and AISI D2 substrates using DC magnetron sputtering in a gas mixture of N_2 and Ar. The effects of the variation of the Ar/N_2 ratio on the chemical composition, structure, surface morphology, residual stress and mechanical properties of the Ti-Cr-N films were investigated.

Based on this study, the growing process of Ti-Cr-N coatings is divided into three distinct stages depending on the Ar/N_2 ratio. The hardness and Young's modulus were related to the structure evolution and compressive residual stress for the three stages of the film growth.

For the films prepared at low values of Ar/N_2 ratio (Stage I, Ar/N_2 = 1 to 1.4), the composition and structure reveal rich metallic nitrides films with a slight increase in residual stress, hardness and Young's modulus. The films corresponding to the intermediate gas ratio (Stage II, Ar/N_2 = 1.4 to 3) presented an increase of their hardness and Young's modulus with the Ar/N_2 ratio. Maximum hardness and Young's modulus of 24 GPa and 255 GPa were respectively reached at $Ar/N_2 = 3$ while the residual stress was relaxed and a smoother surface was observed. This optimum in properties is attributed to the combined effect of film densification and the strengthening mechanism of the grain boundaries. Finally, the films prepared with the highest gas ratio (Stage III, $Ar/N_2 >$ 3), lead to the re-sputtering of the surface, an increase of the surface roughness and compressive residual stress. The dominant metallic

Table 3
Surface roughness and mechanical proprieties of Ti-Cr-N films.

Ar/N_2 ratio	Roughness (RMS) (nm)	Hardness (H) (GPa)	Young's modulus (E) (GPa)	Plastic deformation resistance (H^3/E^2) (GPa)
1.0	3.8 ± 0.1	10 ± 1	190 ± 19	0.03
1.4	4.4 ± 0.1	13 ± 2	215 ± 22	0.05
2.0	2.4 ± 0.1	22 ± 1	250 ± 20	0.17
3.0	1.9 ± 0.1	24 ± 2	255 ± 6	0.21
4.0	2.7 ± 0.1	15 ± 3	245 ± 16	0.06

Table 4
Hardness and Young modulus reported in different works.

	Hardness (GPa)	Young module (GPa)
Present study	10–24	190–255
Feng et al. [16]	12.6–25.8	195.6–362.7
Hones et al. [62]	14–18	215–250
Hsieh et al. [63]	23–26	254–293
Akbarzadeh et al. [64]	22.5–26	373–415
Wang et al. [65]	13.9	295

character of the bonding due to the decrease in nitrogen content and hence, decreases its covalency, combined with the excessive densification induced by the higher ion bombardment, leads to a drastic decrease in hardness and Young's modulus of the film obtained for $Ar/N_2 = 4$. It has also been shown that the hardening caused by the densification of the structure with an optimum level of compressive residual stress contributed to a maximum of resistance to plastic deformation (H^3/E^2).

Finally, this study demonstrated that the Ti-Cr-N coatings are very sensitive to the variation of the gas ratio Ar/N_2 and showed a wide range of mechanical properties.

CRediT authorship contribution statement

Abdelkrim Kehal: Investigation, Writing – original draft. **Nadia Saoula:** Supervision, Writing – review & editing. **Seddik-El-Hak Abaidia:** Supervision, Writing – review & editing. **Corinne Nouveau:** Supervision, Writing – review & editing.

Declaration of competing interest

All authors have no conflict of interest to declare.

Acknowledgements

The authors are grateful to the MESRS (Ministère de l'Enseignement Supérieur et de la Recherche Scientifique), of Algeria, for financial support. They also want to thank Mr. Khelladi, Mohamed Redha from LCIMN (Laboratoire de Chimie, Ingénierie Moléculaire et Nanostructures) of University Ferhat- Abbas, Sétif in Algeria, for his technical expertise.

References

[1] Z. Zhang, J. Chen, G. He, G. Yang, Fatigue and mechanical behavior of Ti-6Al-4V alloy with CrN and TiN coating deposited by magnetic filtered cathodic vacuum arc process, Coatings. 9 (2019) 1–13, https://doi.org/10.3390/coatings9100689.
[2] C. Paksunchai, S. Denchitcharoen, S. Chaiyakun, P. Limsuwan, Effect of sputtering current on structure and morphology of (Ti 1-xCrx)N thin films deposited by reactive unbalanced magnetron co-sputtering, Procedia Eng. 32 (2012) 875–881, https://doi.org/10.1016/j.proeng.2012.02.026.
[3] C. Paksunchai, S. Denchitcharoen, S. Chaiyakun, P. Limsuwan, Effect of sputtering current on structure and morphology of (Ti 1-x Cr x) N thin films deposited by reactive unbalanced magnetron co-sputtering, Procedia Eng. 32 (2012) 875–881, https://doi.org/10.1016/j.proeng.2012.02.026.
[4] G. Mendoza-Leal, C. Hernandez-Navarro, J. Restrepo, M. Flores-Martinez, E. Rodríguez, E. García, Tribological performance of ternary TiMN films (M=AL, B, and Cr) deposited by cathodic arc on M2 steel, Mater. Res. Soc. Adv. 3 (2018) 3675–3681, https://doi.org/10.1557/adv.2018.605.
[5] K. Taweesup, P. Visuttipitukul, N. Yongvanich, G. Lothongkum, Corrosion behavior of Ti-Cr-N coatings on tool steel substrates prepared using DC magnetron sputtering at low growth temperatures, Surf. Coat. Technol. 358 (2019) 732–740, https://doi.org/10.1016/j.surfcoat.2018.11.082.
[6] X. Suo, C. Guo, D. Kong, L. Wang, Corrosion behaviour of TiN and CrN coatings produced by magnetron sputtering process on aluminium alloy, Int. J. Electrochem. Sci. 14 (2019) 826–837. doi:10.20964/2019.01.81.
[7] J.Z. Kong, T.J. Hou, Q.Z. Wang, L. Yin, F. Zhou, Z.F. Zhou, L.K.Y. Li, Influence of titanium or aluminum doping on the electrochemical properties of CrN coatings in artificial seawater, Surf. Coat. Technol. 307 (2016) 118–124, https://doi.org/10.1016/j.surfcoat.2016.08.036.
[8] J.J. Nainaparampil, J.S. Zabinski, A. Korenyi-both, Formation and characterization of multiphase film properties of (Ti-Cr)N formed by cathodic arc deposition, 333 (1998) 88–94.
[9] M.M. Quazi, M. Ishak, A. Arslan, M. Nasir Bashir, I. Ali, Scratch adhesion and wear failure characteristics of PVD multilayer CrTi/CrTiN thin film ceramic coating deposited on AA7075-T6 aerospace alloy, J. Adhes. Sci. Technol. 32 (2018) 625–641, https://doi.org/10.1080/01694243.2017.1373988.
[10] P. Hones, R. Sanjinés, F. Lévy, Sputter deposited chromium nitride based ternary compounds for hard coatings, Thin Solid Films 332 (1998) 240–246, https://doi.org/10.1016/S0040-6090(98)00992-4.
[11] M. Huang, Z. Chen, M. Wang, Y. Li, Y. Wang, Microstructure and properties of TiCrN coatings by arc ion plating, Surf. Eng. 32 (2016) 284–288, https://doi.org/10.1179/1743294415Y.0000000039.
[12] J. Musil, P. Karvánková, J. Kasl, Hard and superhard Zr-Ni-N nanocomposite films, Surf. Coat. Technol. 139 (2001) 101–109, https://doi.org/10.1016/S0257-8972(01)00989-6.
[13] V.M. Vishnyakov, V.I. Bachurin, K.F. Minnebaev, R. Valizadeh, D.G. Teer, J.S. Colligon, V. V Vishnyakov, V.E. Yurasova, Ion assisted deposition of titanium chromium nitride, Thin Solid Films. 497 (2006) 189–195. doi:https://doi.org/10.1016/j.tsf.2005.05.005.
[14] K. Sarakinos, J. Alami, S. Konstantinidis, High power pulsed magnetron sputtering: a review on scientific and engineering state of the art, Surf. Coat. Technol. 204 (2010) 1661–1684, https://doi.org/10.1016/j.surfcoat.2009.11.013.
[15] S. Chen, D. Luo, G. Zhao, Investigation of the properties of TixCr1-xN coatings prepared by cathodic arc deposition, Phys. Procedia 50 (2013) 163–168, https://doi.org/10.1016/j.phpro.2013.11.027.
[16] X. Feng, H. Zhou, Z. Wan, K. Zhang, Effect of Ti content on structure and mechanical properties of Cr–Ti–N films, Surf. Eng. 33 (2017) 619–625, https://doi.org/10.1080/02670844.2016.1212531.
[17] A. Kosari Mehr, M.R. Zamani Meymian, A. Kosari Mehr, Nanoindentation and nanoscratch studies of submicron nanostructured Ti/TiCrN bilayer films deposited by RF-DC co-sputtering method, Ceram. Int. 44 (2018) 21825–21834, https://doi.org/10.1016/j.ceramint.2018.08.288.
[18] M.R.Z.M. Abbas Kosari Mehr, Reza Babaei, Ali Kosari Mehr, Raman and ultraviolet–visible spectroscopy of titanium chromium nitride thin films, Surf. Eng. 0844 (2020) 1–6. doi:https://doi.org/10.1080/02670844.2020.1746493.
[19] L. Aissani, A. Alhussein, C. Nouveau, L. Ghelani, M. Zaabat, Influence of film thickness and Ar-N 2 plasma gas on the structure and performance of sputtered vanadium nitride coatings, Surf. Coatings Technol. J. 378 (2019). doi:https://doi.org/10.1016/j.surfcoat.2019.124948.
[20] C. Oliver, M. Pharr, An improved technique for determining hardness and elastic modulus using load and displacement sensing indentation experiments, J. Mater. Res. 7 (1992) 1564–1583, https://doi.org/10.1557/JMR.1992.1564.
[21] J.S. Jeng, C.H. Liu, J.S. Chen, Effects of substrate bias and nitrogen flow ratio on the resistivity, composition, crystal structure, and reflectance of reactively sputtered hafnium-nitride film, J. Alloys Compd. 486 (2009) 649–652, https://doi.org/10.1016/j.jallcom.2009.07.023.
[22] S. Alaksanasuwan, A. Buranawong, N. Witit-Anun, Preparation and characterization of nanostructured TiCrN thin films deposited from Ti-Cr mosaic target by reactive DC magnetron sputtering, J. Phys. Conf. Ser. 2021 (1719), 012072, https://doi.org/10.1088/1742-6596/1719/1/012072.
[23] P. Dubey, V. Arya, S. Srivastava, D. Singh, R. Chandra, Effect of nitrogen flow rate on structural and mechanical properties of Zirconium Tungsten Nitride (Zr-W-N) coatings deposited by magnetron sputtering, Surf. Coat. Technol. 236 (2013) 182–187, https://doi.org/10.1016/j.surfcoat.2013.09.045.
[24] I. Safi, Recent aspects concerning DC reactive magnetron sputtering of thin films: a review, Surf. Coat. Technol. (2000) 203–219.
[25] H.A. Castillo, W.D. La Cruz, The role of the nitrogen flow rate on the transport properties of CrN thin films produced by DC magnetron sputtering, Surf. Coat. Technol. (2017), https://doi.org/10.1016/j.surfcoat.2017.11.009.
[26] S.L.P. Patsalas, C. Gravalidis, Surface kinetics and subplantation phenomena affecting the texture, morphology, stress, and growth evolution of titanium nitride films, J. Appl. Phys. 96 (2004) 6234–6235, https://doi.org/10.1063/1.1811389.
[27] A.V. Chernogor, F.F. Klimashin, A.O. Volkhonskii, I.V. Blinkov, P.H. Mayrhofer, The impact of Ni and Mo on growth-morphology and mechanical properties of arc evaporated Ti-Cr-N hard coatings, Surf. Coat. Technol. 377 (2019) 124917, https://doi.org/10.1016/j.surfcoat.2019.124917.
[28] F. Vaz, P. Carvalho, L. Cunha, L. Rebouta, C. Moura, E. Alves, Property change in ZrN x O y thin films: effect of the oxygen fraction and bias voltage, Thin Solid Films 470 (2004) 11–17, https://doi.org/10.1016/j.tsf.2004.06.191.
[29] V.V. Uglov, V.M. Anishchik, S.V. Zlotski, I.D. Feranchuk, T.A. Alexeeva, A. Ulyanenkov, J. Brechbuehl, A.P. Lazar, Composition and phase stability upon annealing of gradient nitride coatings, Surf. Coat. Technol. 202 (2008) 2389–2393, https://doi.org/10.1016/j.surfcoat.2007.11.018.
[30] J. Lin, W.D. Sproul, J.J. Moore, Z.L. Wu, S.L. Lee, Effect of negative substrate bias voltage on the structure and properties of CrN films deposited by modulated pulsed power (MPP) magnetron sputtering, J. Phys. D. Appl. Phys. 44 (2011) 425305, https://doi.org/10.1088/0022-3727/44/42/425305.
[31] S. Klima, H. Hruby, J. Julin, M. Burghammer, J.F. Keckes, C. Mitterer, R. Daniel, Evolution of structure and residual stress of a fcc/hex-AlCrN multi- layered system upon thermal loading revealed by cross-sectional X-ray nano-diffraction, 162 (2019) 55–66. doi:https://doi.org/10.1016/j.actamat.2018.09.031.
[32] C. Paksunchai, S. Denchitcharoen, S. Chaiyakun, P. Limsuwan, Growth and Characterization of Nanostructured TiCrN Films Prepared by DC Magnetron Cosputtering, 2014 (2014).
[33] C. Kainz, N. Schalk, M. Tkadletz, C. Mitterer, C. Czettl, Microstructure and mechanical properties of CVD TiN/TiBN multilayer coatings, Surf. Coat. Technol. 370 (2019) 311–319, https://doi.org/10.1016/j.surfcoat.2019.04.086.

[34] Z. Qi, Z. Wu, D. Zhang, B. Wei, J. Wang, Z. Wang, Effect of Sputtering Power on the Chemical Composition, Microstructure and Mechanical Properties of CrNx Hard Coatings Deposited by Reactive Magnetron Sputtering, Elsevier Ltd., 2017, https://doi.org/10.1016/j.vacuum.2017.08.036.

[35] P. V Kiryukhantsev-korneev, D. V Shtansky, M.I. Petrzhik, E.A. Levashov, B.N. Mavrin, Thermal stability and oxidation resistance of Ti – B – N, Ti – Cr – B – N, Ti – Si – B – N and Ti – Al – Si – B – N films, Surf. Coat. Technol. 201 (2007) 6143–6147. doi:https://doi.org/10.1016/j.surfcoat.2006.08.133.

[36] H.C. Barshilia, K.S. Rajam, Raman spectroscopy studies on the thermal stability of TiN, CrN, TiAlN coatings and nanolayered TiN/CrN, TiAlN/CrN multilayer coatings, J. Mater. Res. (2004), https://doi.org/10.1557/JMR.2004.0444.

[37] R.S. De Freitas, B.C. Viana, F. Eroni, P. Santos, P. Nascente, D.A. Tallarico, V.R. Mastelaro, Influence of the plasma nitriding conditions on the chemical and morphological characteristics of TiN coatings deposited on silicon, 37 (2018) 44–53. doi:10.17563/rbav.v37i2.1083.

[38] N.K. Ponon, D.J.R. Appleby, E. Arac, P.J. King, S. Ganti, K.S.K. Kwa, A. O'Neill, Effect of deposition conditions and post deposition anneal on reactively sputtered titanium nitride thin films, Thin Solid Films 578 (2015) 31–37, https://doi.org/10.1016/j.tsf.2015.02.009.

[39] E. György, A. Pérez del Pino, G. Sauthier, A. Figueras, F. Alsina, J. Pascual, Structural, morphological and local electric properties of TiO2 thin films grown by pulsed laser deposition, J. Phys. D. Appl. Phys. 40 (2007) 5246–5251, https://doi.org/10.1088/0022-3727/40/17/035.

[40] R. Kaiser, Raman scattering, superconductivity, and phonon density of states of stoichiometric and nonstoichiometric TiN, Phys. Rev. B. 17 (1978).

[41] Y.H. Cheng, B.K. Tay, S.P. Lau, X. Shi, Raman spectroscopy and x-ray diffraction studies of (Ti,Al)N films deposited by filtered cathodic vacuum arc at room temperature, J. Appl. Phys. 89 (2001) 6192–6197, https://doi.org/10.1063/1.1352564.

[42] J. Lin, J.J. Moore, B. Mishra, M. Pinkas, W.D. Sproul, J.A. Rees, Effect of asynchronous pulsing parameters on the structure and properties of CrAlN films deposited by pulsed closed field unbalanced magnetron sputtering (P-CFUBMS), Surf. Coat. Technol. 202 (2008) 1418–1436, https://doi.org/10.1016/j.surfcoat.2007.06.068.

[43] H. Wang, S. Zhang, Y. Li, D. Sun, Bias effect on microstructure and mechanical properties of magnetron sputtered nanocrystalline titanium carbide thin films, Thin Solid Films 516 (2008) 5419–5423, https://doi.org/10.1016/j.tsf.2007.07.022.

[44] Z.J. Liu, N. Jiang, Y.G. Shen, Y.W. Mai, Atomic force microscopy study of surface roughening of sputter-deposited TiN thin films, J. Appl. Phys. 92 (2002) 3559–3563, https://doi.org/10.1063/1.1504497.

[45] Y. Liu, Y. Zang, G. Wei, J. Li, X. Fan, C. Cheng, Stress and structural studies of ZnO thin films on polymer substrate under different RF powered conditions, Mater. Lett. 63 (2009) 2597–2599, https://doi.org/10.1016/j.matlet.2009.08.027.

[46] C.W. Zou, H.J. Wang, M. Li, C.S. Liu, L.P. Guo, D.J. Fu, Characterization and properties of CrN films deposited by ion-source-enhanced middle frequency magnetron sputtering, Vaccum. 83 (2009) 1086–1090, https://doi.org/10.1016/j.vacuum.2008.12.007.

[47] M. Griepentrog, B. Mackrodt, G. Mark, T. Linz, Properties of TiN hard coatings prepared by unbalanced magnetron sputtering and cathodic arc deposition using a uni- and bipolar pulsed bias voltage, Surf. Coat. Technol. 74–75, Par (1995) 326–332. doi:https://doi.org/10.1016/0257-8972(95)08369-3.

[48] P. Dubey, G. Martinez, S. Srivastava, R. Chandra, C.V. Ramana, Effect of bias induced microstructure on the mechanical properties of nanocrystalline zirconium tungsten nitride coatings, Surf. Coat. Technol. 313 (2017) 121–128, https://doi.org/10.1016/j.surfcoat.2017.01.067.

[49] D.E. Wolfe, B.M. Gabriel, M.W. Reedy, Nanolayer (Ti,Cr)N coatings for hard particle erosion resistance, Surf. Coat. Technol. 205 (2011) 4569–4576, https://doi.org/10.1016/j.surfcoat.2011.03.121.

[50] S. Jena, R.B. Tokas, J.S. Misal, K.D. Rao, D.V. Udupa, S. Thakur, N.K. Sahoo, Effect of O_2/Ar gas flow ratio on the optical properties and mechanical stress of sputtered HfO2 thin films, Thin Solid Films 592 (2015) 135–142, https://doi.org/10.1016/j.tsf.2015.08.062.

[51] N.R. Shamsutdinov, A.J. Böttger, F.D. Tichelaar, The effect of Cu interlayers on grain size and stress in sputtered Fe–Cu multilayered thin films, Scr. Mater. 54 (2006) 1727–1732, https://doi.org/10.1016/j.scriptamat.2006.02.008.

[52] B.W. Sheldon, A. Rajamani, A. Bhandari, E. Chason, S.K. Hong, B.W. Sheldon, A. Rajamani, A. Bhandari, E. Chason, S.K. Hong, Competition between tensile and compressive stress mechanisms during Volmer-Weber growth of aluminum nitride film, J. Appl. Phys. (2005) 043509, https://doi.org/10.1063/1.1994944.

[53] J.A. Floro, S.J. Hearne, J.A. Hunter, P. Kotula, E. Chason, S.C. Seel, C.V. Thompson, The dynamic competition between stress generation and relaxation mechanisms during coalescence of Volmer-Weber thin films, J. Appl. Phys. 89 (2001) 4886–4897, https://doi.org/10.1063/1.1352563.

[54] S. Zhao, F. Ma, Z. Song, K. Xu, The growth behavior and stress evolution of sputtering-deposited LaNiO3 thin films, Mater. Sci. Eng. A 474 (2008) 134–139, https://doi.org/10.1016/j.msea.2007.04.004.

[55] M. Wen, Q.N. Meng, W.X. Yu, W.T. Zheng, S.X. Mao, M.J. Hua, Growth, stress and hardness of reactively sputtered tungsten nitride thin films, Surf. Coat. Technol. 205 (2010) 1953–1961, https://doi.org/10.1016/j.surfcoat.2010.08.082.

[56] J. Tranchant, P.Y. Tessier, J.P. Landesman, M.A. Djouadi, B. Angleraud, P. O. Renault, B. Girault, P. Goudeau, Relation between residual stresses and microstructure in Mo(Cr) thin films elaborated by ionized magnetron sputtering, Surf. Coat. Technol. 202 (2008) 2247–2251, https://doi.org/10.1016/j.surfcoat.2007.07.030.

[57] C.A. Davis, A simple model for the formation of compressive stress in thin films by ion bombardment, Thin Solid Films 226 (1993) 30–34, https://doi.org/10.1016/0040-6090(93)90201-Y.

[58] H. Windischmann, An intrinsic stress scaling law for polycrystalline thin films prepared by ion beam sputtering, J. Appl. Phys. 62 (1987) 1800–1807, https://doi.org/10.1063/1.339560.

[59] K. Zhang, M. Wen, Q.N. Meng, C.Q. Hu, X. Li, C. Liu, W.T. Zheng, Effects of substrate bias voltage on the microstructure, mechanical properties and tribological behavior of reactive sputtered niobium carbide films, Surf. Coat. Technol. 212 (2012) 185–191, https://doi.org/10.1016/j.surfcoat.2012.09.046.

[60] J. Huang, F. Ouyang, G. Yu, Effect of film thickness and Ti interlayer on the structure and properties of nanocrystalline TiN thin films on AISI D2 steel, Surf. Coat. Technol. 201 (2007) 7043–7053, https://doi.org/10.1016/j.surfcoat.2007.01.012.

[61] Y. Shi, S. Long, S. Yang, F. Pan, Structural and tribological properties of CrTiAlN coatings on Mg alloy by closed-field unbalanced magnetron sputtering ion plating, Appl. Surf. Sci. 254 (2008) 7342–7350, https://doi.org/10.1016/j.apsusc.2008.05.338.

[62] P. Hones, R. Sanjinés, F. Lévy, Sputter deposited chromium nitride based ternary compounds for hard coatings, Thin Solid Films 332 (1998) 240–246, https://doi.org/10.1016/S0040-6090(98)00992-4.

[63] J.H. Hsieh, W.H. Zhang, C. Li, C.Q. Sun, Characterization of (Tix Cr0.6-x) N0.4 coatings and their tribological behaviors against an epoxy molding compound, Surf. Coat. Technol. 146–147 (2001) 331–337, https://doi.org/10.1016/S0257-8972(01)01401-3.

[64] M. Akbarzadeh, A. Shafyei, H.R. Salimijazi, Characterization of TiN, CrN and (Ti, Cr) N coatings deposited by cathodic ARC evaporation, Int. J. Eng. 27 (2014) 1127–1132, https://doi.org/10.5829/idosi.ije.2014.27.07a.14.

[65] Q. Wang, F. Zhou, J. Yan, Evaluating mechanical properties and crack resistance of CrN, CrTiN, CrAlN and CrTiAlN coatings by nanoindentation and scratch tests, Surf. Coat. Technol. 285 (2016) 203–213, https://doi.org/10.1016/j.surfcoat.2015.11.040.

[66] P. Hones, R. Sanjinés, F. Lévy, Sputter deposited chromium nitride based ternary compounds for hard coatings, Thin Solid Films 332 (1998) 240–246, https://doi.org/10.1016/S0040-6090(98)00992-4.

[67] K. Holmberg, H. Ronkainen, A. Matthews, Tribology of thin coatings, Ceram. Int. 26 (2000) 787–795, https://doi.org/10.1016/S0272-8842(00)00015-8.

[68] L. Wang, G. Zhang, R.J.K. Wood, S.C. Wang, Q. Xue, Fabrication of CrAlN nanocomposite fi lms with high hardness and excellent anti-wear performance for gear application, Surf. Coat. Technol. 204 (2010) 3517–3524, https://doi.org/10.1016/j.surfcoat.2010.04.014.

[69] G. Carter, Surface roughening during ion-assisted film deposition, Thin Solid Films 322 (1998) 177–187, https://doi.org/10.1016/S0040-6090(97)01012-2.

[70] A. Cavaleiro, B. Trindade, M.T. Vieira, The Influence of the Addition of a Third Element on the Structure and Mechanical Properties of Transition-Metal-Based Nanostructured Hard Films: Part I—Nitrides, Mech. Eng. (2006) 315–346. doi:A. Cavaleiro, J.T.M. De Hosson, eds., Nanostructured Coatings, Springer New York, New York, NY, 2006.

[71] S. Yu, Q. Zeng, A.R. Oganov, G. Frapper, L. Zhang, Phase stability, chemical bonding and mechanical properties of titanium nitrides: a first-principles study, Phys. Chem. Chem. Phys. 17 (2015) 11763–11769, https://doi.org/10.1039/c5cp00156k.

[72] Y.D. Su, C.Q. Hu, M. Wen, C. Wang, D.S. Liu, W.T. Zheng, Effects of bias voltage and annealing on the structure and mechanical properties of WC0.75N0.25 thin films, J. Alloys Compd. 486 (2009) 357–364, https://doi.org/10.1016/j.jallcom.2009.06.147.

[73] H. Zegtouf, N. Saoula, M. Azibi, L. Bait, N. Madaoui, M.R. Khelladi, M. Kechouane, Influence of substrate bias voltage on structure, mechanical and corrosion properties of ZrO2 thin films deposited by reactive magnetron sputter deposition, Surf. Coat. Technol. 393 (2020) 125821, https://doi.org/10.1016/j.surfcoat.2020.125821.

[74] Y.X. Ou, J. Lin, H.L. Che, J.J. Moore, W.D. Sproul, M.K. Lei, Mechanical and tribological properties of CrN/TiN multilayer coatings deposited by pulsed dc magnetron sputtering, Thin Solid Films 594 (2015) 147–155, https://doi.org/10.1016/j.tsf.2015.09.067.

[75] H.A. Macías, L. Yate, L.E. Coy, J. Olaya, W. Aperador, Effect of nitrogen flow ratio on microstructure, mechanical and tribological properties of TiWSiNx thin film deposited by magnetron co-sputtering, Appl. Surf. Sci. (2018), https://doi.org/10.1016/j.apsusc.2018.06.129.